



Contents lists available at ScienceDirect

Journal of Power Sources

journal homepage: [www.elsevier.com/locate/jpowsour](http://www.elsevier.com/locate/jpowsour)

## Single-step synthesis of highly conductive $\text{Na}_3\text{PS}_4$ solid electrolyte for sodium all solid-state batteries

Han Nguyen<sup>a</sup>, Abhik Banerjee<sup>a</sup>, Xuefeng Wang<sup>a</sup>, Darren Tan<sup>a</sup>, Erik A. Wu<sup>a</sup>, Jean-Marie Doux<sup>a</sup>, Ryan Stephens<sup>c</sup>, Guy Verbist<sup>d</sup>, Ying Shirley Meng<sup>a,b,\*</sup>

<sup>a</sup> Department of NanoEngineering, University of California, San Diego, La Jolla, CA, 92093, USA

<sup>b</sup> Sustainable Power & Energy Center (SPEC), University of California, San Diego, La Jolla, CA, 92093, USA

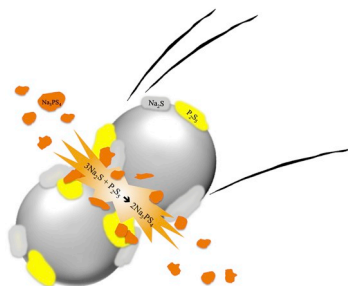
<sup>c</sup> Shell International Exploration & Production Inc, USA

<sup>d</sup> Shell Global Solutions International BV, USA

### HIGHLIGHTS

- Single-step synthesis of highly conductive sodium solid-state electrolyte.
- Facile synthesis process for large batch production of solid-state electrolyte.
- All solid-state battery constructed with  $\text{Na}_3\text{PS}_4$ .

### GRAPHICAL ABSTRACT



### ARTICLE INFO

#### Keywords:

Ball milling  
Sodium battery  
Solid-state electrolyte  
Sulfide  
Synthesis  
 $\text{Na}_3\text{PS}_4$

### ABSTRACT

$\text{Na}_3\text{PS}_4$  has been demonstrated to be a promising solid electrolyte for all solid-state sodium ion batteries. Its high intrinsic ionic conductivity makes it ideal for high power battery applications. Although much research has been conducted on studying its structural and electrochemical properties, there is still no consensus on an optimal synthesis protocol despite a variety of reported  $\text{Na}_3\text{PS}_4$  synthesis methods available. Here, we investigate the key parameters required to achieve single-step scalable synthesis of  $\text{Na}_3\text{PS}_4$  solid electrolyte from its starting precursors. We determine that  $\text{Na}_3\text{PS}_4$  solid electrolyte with high ionic conductivity ( $\sim 0.2 \text{ mS cm}^{-1}$ ) can be easily achieved in 20 min using a single synthesis step, representing a significant improvement over other existing energy-intensive multiple-step methods. The all solid-state battery constructed with this highly conductive  $\text{Na}_3\text{PS}_4$  is able to deliver  $185 \text{ mAh g}^{-1}$  capacity on the first discharge and excellent rate performance with a  $\text{TiS}_2$  cathode and a  $\text{Na}_{15}\text{Sn}_4$  anode.

### 1. Introduction

All solid-state batteries (ASSB) are regarded as a promising

alternative to replace state-of-the-art liquid electrolyte-based batteries. This is due to their improved safety from the use of non-flammable components, wider operating temperature range, as well as the

\* Corresponding author. Department of NanoEngineering, University of California, San Diego, La Jolla, CA, 92093, USA.

E-mail address: [shmeng@ucsd.edu](mailto:shmeng@ucsd.edu) (Y.S. Meng).

<https://doi.org/10.1016/j.jpowsour.2019.05.031>

Received 21 February 2019; Received in revised form 18 April 2019; Accepted 9 May 2019

0378-7753/© 2019 Elsevier B.V. All rights reserved.

**Table 1**  
Summarized Synthesis conditions of the Na<sub>3</sub>PS<sub>4</sub> SSE.

Ball Mill Manufacturer	Na <sub>2</sub> S Source	Media	Jar Size (mL)	Ball Size (mm)	Speed (RPM)	Total Milling Time	Heating Treatment	Conductivity (S.cm <sup>-1</sup> )	Ref.
Retsch	Sigma Aldrich	ZrO <sub>2</sub>	50	10	600	20 min	–	2 × 10 <sup>-4</sup>	This work
Fritsch	Sigma Aldrich	ZrO <sub>2</sub>	45	4	510	20 h	270 °C, 2 h	1 × 10 <sup>-4</sup>	[19]
Fritsch	Sigma Aldrich	ZrO <sub>2</sub>	80	3	500	48 h	270 °C, 12 h	1.5 × 10 <sup>-4</sup>	[20,21]
Fritsch	Sigma Aldrich	ZrO <sub>2</sub>	45	4	510	15 h	220 °C, 2 h	1 × 10 <sup>-4</sup>	[22–24]
Fritsch	Nagao	ZrO <sub>2</sub>	45	4	510	1.5–8 h	270 °C, 2 h	1.7–4 × 10 <sup>-4</sup>	[25,26]
Retsch PM400	Aladdin Chem	ZrO <sub>2</sub>	50	–	500	13.5 h	270 °C, 2 h	1.7 × 10 <sup>-4</sup>	[27]
Fritsch	Sigma Aldrich	ZrO <sub>2</sub>	50	3	510	48 h	270 °C, 48 h	0.4 × 10 <sup>-4</sup>	[28]
Fritsch	Sigma Aldrich	ZrO <sub>2</sub>	50	3	510	20 h	270 °C, 1 h	1 × 10 <sup>-4</sup>	[29]
Across International	Alfa Aesar	Agate	–	–	510	15 h	270 °C, 2 h	2 × 10 <sup>-4</sup>	[30]
Fritsch	–	ZrO <sub>2</sub>	45	10	–	10 h	250 °C, 2 h	–	[31]

potential to achieve high energy density by enabling metallic anodes [1]. The key component of an ASSB is its solid electrolyte, which serves as a physical barrier between the cathode and anode, and allows transport of active ion(s) between them.

Despite the rich research history of solid-state electrolytes (SSEs) for energy storage and conversion materials applications [2], widespread adoption of SSEs has fallen behind their liquid counterparts, mainly due to their inferior power capabilities and expensive processability. However, recent discoveries of some sulfide SSEs such as Li<sub>10</sub>GeP<sub>2</sub>S<sub>12</sub> and Na<sub>3</sub>PS<sub>4</sub> are challenging this status quo. As a sulfide-based SSE, it can be synthesized and sintered at low temperatures compared to oxide-based analogs, significantly lowering the processing cost. Furthermore, with its power capabilities rivaling that of liquid electrolytes (>10 mS cm<sup>-1</sup>), sulfide-based SSE are slated to front the future of energy storage technologies [3].

Lithium-ion containing electrolytes are undoubtedly the most successful chemistries to date. However, taking material abundance into consideration, lithium sources are relatively limited and thus the lithium compounds are costly to produce. In contrast, sodium sources are considered virtually inexhaustible and readily accessible [4,5]. This makes sodium battery chemistries attractive and justifies their ongoing development mirroring that of lithium ion batteries [6–12]. Until recently, the most widely adopted sodium solid electrolytes are NASICON and β-Alumina, with commercial applications of the latter in niche markets [13–17]. However, demands for high power and cheaper processing have made Na<sub>3</sub>PS<sub>4</sub> a more promising solid-state electrolyte (SSE) candidate for energy storage and conversion applications.

The tetragonal polymorph Na<sub>3</sub>PS<sub>4</sub>, with the  $P\bar{4}2_1c$  space group, was first studied in detail by Jansen et al. They suggested that a high temperature phase exists after observing a sharp change in the material's Arrhenius curve [18]. Hayashi et al. later stabilized this high temperature phase and determined it to be cubic Na<sub>3</sub>PS<sub>4</sub>, where they showed the superior sodium ion conductivity of cubic Na<sub>3</sub>PS<sub>4</sub> compared to its tetragonal polymorph [19]. To achieve this, Hayashi et al. used ball milling to form an amorphous phase from crystalline precursors and subsequent heat treatment to stabilize the cubic Na<sub>3</sub>PS<sub>4</sub> phase at room temperature. This two-step method, of ball milling followed by heat treatment represents the common general approach taken by almost all reports in the literature [19–31]. Table 1 summarizes all reported studies on Na<sub>3</sub>PS<sub>4</sub> with their respective synthesis conditions. As shown in Table 1, there are still wide variations amongst its specific parameters, such as: precursor source, grinding media size and material, rotation speeds, milling time and heat treatment durations. As such, there is no established consensus on the parameters used to consistently achieve the desired properties of cubic Na<sub>3</sub>PS<sub>4</sub>, such as high conductivity on the order of 10<sup>-4</sup> S cm<sup>-1</sup>.

In this work, we systematically optimize synthesis conditions of Na<sub>3</sub>PS<sub>4</sub> to produce the target phase and conductivity using a single-step synthesis technique. The synthesis conditions include total ball milling time, rotation speed, ball size, and secondary heat treatment. The results

show that ball milling alone is sufficient to produce the Na<sub>3</sub>PS<sub>4</sub> with the highest ionic conductivity. Using this material as a solid-state electrolyte, the TiS<sub>2</sub> cell is able to deliver 185 mAh g<sup>-1</sup> and a modest capacity evolution with different current densities.

## 2. Experimental methods

### 2.1. Ball milling of Na<sub>3</sub>PS<sub>4</sub>

Na<sub>2</sub>S (Sigma Aldrich 98% or Nagao 99.6%) and P<sub>2</sub>S<sub>5</sub> (Sigma Aldrich 99%) was loaded into a milling jar at a molar ratio of 75:25, respectively. The total mass of the mixture was 1 g. The milling jar volume is 50 mL with an inner lining made of Y–ZrO<sub>2</sub> (Retsch). The jar was preloaded with ZrO<sub>2</sub> grinding media where an 8.7:1 jar to grinding-media volume ratio was maintained. The loaded jar was sealed in an Ar-containing glovebox and the milling proceeded under inert conditions using a Retsch PM100 planetary ball mill. Ball milling proceeded at 550 RPM unless stated otherwise. In the case where the effect of heat treatment was evaluated, the samples were loaded into a quartz tube and capped with a rubber septum. The tube was then flame-sealed and heat-treated in a box furnace (Lindberg Blue M). The temperature was ramped from room temperature to 270 °C at a rate of 10 °C min<sup>-1</sup> and held for two hours at temperature. The sealed tube was then quenched in ice water and the sample extracted for characterization.

### 2.2. Electrochemical impedance spectroscopy (EIS)

The conductivity of the solid electrolyte material was evaluated by EIS. Pellets were formed with a custom-made PEEK die mold and titanium plungers. Na<sub>3</sub>PS<sub>4</sub> powder was loaded into the 10 mm diameter PEEK pellet die and pressed at 360 MPa at room temperature. The two titanium plungers were used as blocking current collectors for the EIS measurements. Data was collected with a Solartron 1260 frequency response analyzer, with an excitation potential of 30 mV and a frequency range between 1 MHz and 1 Hz.

### 2.3. Materials characterization

All X-ray diffraction (XRD) samples were loaded into boron-rich 0.5 mm diameter glass capillary tubes (Charles Supper) and flame-sealed to prevent exposure to ambient atmosphere. The samples were measured on a Bruker Kappa goniometer equipped with a Bruker Vantec 500 detector. XRD data was collected using Cu K<sub>α</sub> radiation at 45 kV and 50 mA, over a 2θ range of 10–70°. Rietveld refinement was conducted using the GSAS software suite [32,33]. Raman (Renishaw inVia/Bruker Innova) was used with 514 nm illumination, provided by a Modu-Laser 50 mW Ar<sup>+</sup> ion laser. The samples were prepared by placing the powder onto a coverslip and sealed with Kapton tape. Data collection was made through the cover slip side.

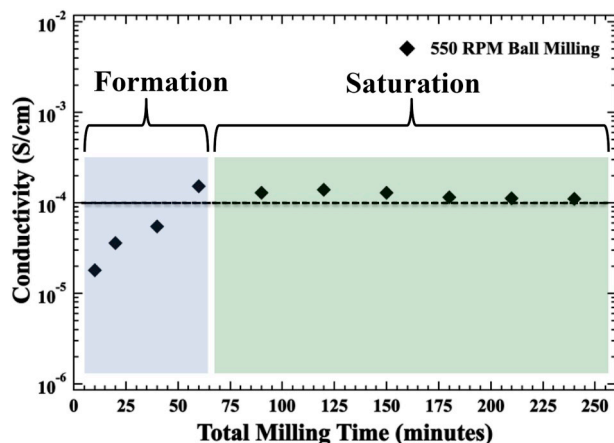


Fig. 1. Conductivity evolution of the ball-milled  $75\text{Na}_2\text{S}-25\text{P}_2\text{S}_5$  mixture as a function of total milling time at 550 RPM with 10 mm grinding media.

#### 2.4. Scanning electron microscopy (SEM)

Iridium was sputtered onto the electronically insulating SSE by an Emitech sputter coater for 7 s with a current of 85 mA. Images of particle morphology and size were taken with a FEI Quanta 250 SEM.

#### 2.5. Electrochemical characterization

DC polarization measurements were made with a Biologic SP-200 potentiostat with a low-current probe attachment. A pellet of  $\text{Na}_3\text{PS}_4$  (ball milled for 1 h at 550 rpm with  $11 \times 10$  mm grinding media) was made in a PEEK die by pressing between titanium plungers at 360 MPa. The steady-state current was collected when varying polarization potentials to determine the electronic conductivity of the solid electrolyte. An all solid-state battery was constructed with  $\text{TiS}_2$  (Sigma Aldrich 99.9%) as the cathode,  $\text{Na}_3\text{PS}_4$  as the electrolyte, and  $\text{Na}_{15}\text{Sn}_4$  alloy as the anode.  $\text{TiS}_2$  was chosen for the cathode as it has sufficient electronic conductivity and does not require the addition of carbon. The anode alloy was formed by ball milling stoichiometric amount of Na and Sn in a 15:4 ratio under inert conditions, as outlined by Tanibata et al. [23]. The alloy anode was chosen over sodium metal because the later is known to form a resistive interphase with  $\text{Na}_3\text{PS}_4$  [34].  $\text{Na}_{15}\text{Sn}_4$  is relatively more stable and used to evaluate the ball-milled  $\text{Na}_3\text{PS}_4$  in an all solid-state cell. The composite cathode material consisted of 1:1 wt ratio of  $\text{TiS}_2$

and  $\text{Na}_3\text{PS}_4$ , mixed together with agate mortar and pestle. The tri-layer all solid-state cell was constructed in a PEEK die mold and pressed to 360 MPa with titanium plungers. The titanium plungers were also used as the current collectors.

### 3. Results and discussion

#### 3.1. Ball milling time

Total ball milling time was the first synthesis parameter investigated in this work, as it presents the largest variation in the literature (Table 1). For this well-controlled exploration, rotational speed was fixed at 550 RPM and the material's conductivity was measured at intermittent ball milling time intervals. The results were collected and are presented in Fig. 1. Two distinct stages of the ball milling process could be observed and assigned, namely the Formation and Saturation stages. During the Formation stage, the ionic conductivity of the SSE increases from  $0.18 \times 10^{-4} \text{ S cm}^{-1}$  to a maximum of  $1.7 \times 10^{-4} \text{ S cm}^{-1}$ , which was achieved within one hour of total ball milling at the given conditions. While in the Saturation stage, the ionic conductivity of the SSE does not increase with any additional milling and suggest the material synthesis has reached steady state. To understand the processes occurring during these two stages, the structural evolution of the mixture at each time interval was analyzed with XRD and Raman spectroscopy (Fig. 2).

XRD and Raman analyses reveal that the ball milling process induces a reaction between starting precursors during the Formation stage, as shown in Fig. 2a and b. The starting mixture of  $\text{Na}_2\text{S}$  and  $\text{P}_2\text{S}_5$  are gradually consumed to form  $\text{Na}_3\text{PS}_4$  and occurs as early as ten minutes into ball milling. In Fig. 2a, markers indicate where cubic and tetragonal  $\text{Na}_3\text{PS}_4$  phases can be identified and vertical dashed lines are used to distinguish the non-overlapping peaks of tetragonal  $\text{Na}_3\text{PS}_4$ . The intense peaks identified as  $\text{Na}_2\text{S}$  are also present with the SSE in the early stages of Formation. After ten minutes of ball milling, the diffraction peaks for  $\text{P}_2\text{S}_5$  are no longer visible; it is presumed that  $\text{P}_2\text{S}_5$  becomes amorphous and thus invisible to diffraction experiments. In this case, Raman spectroscopy was used as a complementary technique to XRD. Fig. 2b depicts the Raman spectroscopy measurements collected on the ball milled sample. The  $\text{Na}_3\text{PS}_4$  exhibits peaks at  $280 \text{ cm}^{-1}$ ,  $411 \text{ cm}^{-1}$ ,  $536 \text{ cm}^{-1}$ , and  $567 \text{ cm}^{-1}$  attributed to the tetrahedral  $\text{PS}_4^{3-}$ . The  $\text{P}_2\text{S}_5$  exhibits Raman peaks at  $159 \text{ cm}^{-1}$ ,  $180 \text{ cm}^{-1}$ ,  $191 \text{ cm}^{-1}$ ,  $197 \text{ cm}^{-1}$ ,  $270 \text{ cm}^{-1}$ ,  $303 \text{ cm}^{-1}$ ,  $385 \text{ cm}^{-1}$ ,  $394 \text{ cm}^{-1}$ ,  $405 \text{ cm}^{-1}$  and was determined to be present during the first ten minutes of ball milling. This shows that  $\text{P}_2\text{S}_5$

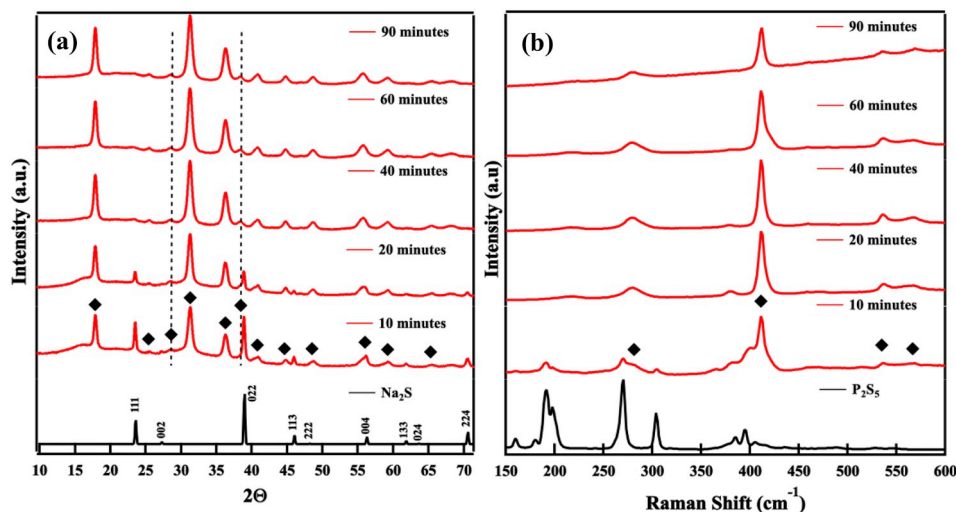


Fig. 2. (a) XRD patterns of mixture at various milling times. (b) Raman spectra of the  $75\text{Na}_2\text{S}-25\text{P}_2\text{S}_5$  mixture at various milling times. Markers indicate overlapping peaks of cubic and tetragonal  $\text{Na}_3\text{PS}_4$  phase and the dashed lines denote peaks from the latter phase.

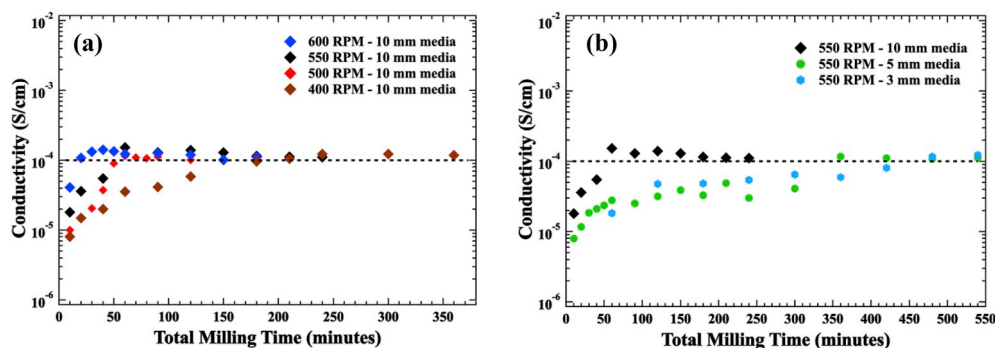


Fig. 3. Evolution of the conductivity of the  $75\text{Na}_2\text{S}-25\text{P}_2\text{S}_5$  mixture during the synthesis, when (a) varying the ball milling speed and (b) varying the grinding media size.

is indeed in the mixture and the reaction of  $\text{Na}_3\text{PS}_4$  was determined to be incomplete during the early stages of Formation. From the XRD patterns in Fig. 2a, the concentrations of  $\text{Na}_3\text{PS}_4$  increases as starting precursors are being consumed; as shown by their decreasing relative peak intensities as ball milling progresses. Once sixty minutes of total ball milling time is reached, the XRD and Raman results show that only  $\text{Na}_3\text{PS}_4$  is present and the starting precursors are completely consumed.

Sodium ion conductivities were also measured in parallel with XRD and Raman data collection at the respective milling intervals. During the Formation stage, the ionic conductivity increases with ball milling from  $0.18 \times 10^{-4} \text{ S cm}^{-1}$ ,  $0.36 \times 10^{-4} \text{ S cm}^{-1}$ ,  $0.55 \times 10^{-4} \text{ S cm}^{-1}$ , until a maximum value of  $1.7 \times 10^{-4} \text{ S cm}^{-1}$  is reached and all of the starting precursors are consumed at the end of the Formation stage. Saturation begins at this stage, meaning any additional ball milling does not improve nor degrade the material's conductivity. Coupled with XRD and Raman, it is evident that there are no more structural changes, secondary phases, or precursor peaks detected with additional ball milling during the Saturation stage. As such, we can conclude that the Saturation stage is synonymous with reaction completion, as only the  $\text{Na}_3\text{PS}_4$  phase is detected. The XRD and Raman results for after ninety minutes of ball milling are not shown for clarity.

Rietveld refinement was performed on the material ball milled for a total of one hour and the results are shown in Fig. S1 and tabulated in Table S1 of the Supporting Information. The main phase was determined to be cubic  $\text{Na}_3\text{PS}_4$  and the minor phase determined to be tetragonal  $\text{Na}_3\text{PS}_4$ , at 91% and 9% weight percent, respectively. The peaks of cubic and tetragonal  $\text{Na}_3\text{PS}_4$  overlap except for the (201) ( $2\theta = 24^\circ$ ) and (212) ( $2\theta = 37^\circ$ ) peaks. These peaks are forbidden in the  $I_{43m}$  space-group (No. 217) for the cubic phase, while they are allowed in the  $P_{421c}$  space group (No. 114) for the tetragonal phase, where the cubic symmetry is broken by the latter phase having a larger c-lattice parameter. The results determined in this work are consistent with Krauskopf et al., where they conducted a detailed structural analysis of the two phases of  $\text{Na}_3\text{PS}_4$  being present in the SSE [20]. Interestingly, all the peaks of the  $\text{Na}_3\text{PS}_4$  are present during the first ten minutes of milling. This suggests that the formation of both cubic and tetragonal  $\text{Na}_3\text{PS}_4$  is simultaneous during the early stages of ball milling. Nonetheless, a higher percentage of cubic  $\text{Na}_3\text{PS}_4$  phase was found at the latter stages and explains the high conductivities measured. The mechanism of this reaction has yet to be well understood and this presents a good direction for future work.

Our results show the crystalline phase  $\text{Na}_3\text{PS}_4$  can be directly obtained from ball milling, which is contrary to findings by Hayashi et al. However, this is consistent with results reported by Berbano et al., where crystalline phases were achieved via both ball milling and melt-quenching with a starting  $\text{Na}_2\text{S}-\text{P}_2\text{S}_5$  mixture at molar ratios of 3 to 1 [19,35]. Further analysis of the material was collected with differential scanning calorimetry (DSC) and is described in Fig. S2 of the Supporting Information. The results are consistent with our XRD and Raman

spectroscopy findings. By forming the desired structure without the need for post-synthesis heating of an amorphous phase, it is expected to reduce the time and energy cost needed to form the desired SSE.

### 3.2. Rotational speed and grinding media size

The influence of the rotational speed and the grinding media size was also investigated. It was found that the rotational speed of ball milling has a direct effect on the time required to complete the Formation stage. From Fig. 3a, increased speeds is shown to reduce the time required to complete the reaction of  $\text{Na}_3\text{PS}_4$  and achieve maximum conductivity: going from 550 RPM to 600 RPM, the synthesis time can be reduced from one hour to as short as twenty minutes. A similar result was observed when the grinding media size was varied and the rotational speed was fixed at 550 RPM and shown in Fig. 3b. The largest media size used was 10 mm diameter balls and maximum conductivity is achieved after one hour of total milling at 550 RPM. Longer milling times were needed as the size of grinding media was reduced, with the smallest grinding media (3 mm in diameter), 500 min of ball milling are required to complete the formation of  $\text{Na}_3\text{PS}_4$ . This can be attributed to the lower kinetic energy of the collisions resulting from the smaller grinding media; a decrease in energy means a longer milling time is required to complete the SSE reaction. It is important to note that the Formation and Saturation stages are always present regardless of which milling parameter is varied.

Ball milling is commonly used as a particle size reduction method to break down coarse materials into fine powders where smaller media sizes are expected to produce finer particles. At the same time it can also make particle sizes more homogenous. As such, SEM was used to examine the morphology and determine the particle size distribution of the  $\text{Na}_3\text{PS}_4$  electrolyte milled with varying media size at the end of each Saturation stage. Representative particles and their particle size distribution (evaluated from a sample size of 320 particles for each grinding media size) are shown in Fig. S3. As shown on the SEM images, the grinding media size does not induce any modification of the morphology of the particles. On the other hand, the particle size distribution (tabulated in Table S2, described by the diameter of 10% (D10), 50% (D50) and 90% (D90) of the particles), is clearly influenced by the grinding media size. It appears that when switching from 10 to 3 mm grinding media, D10 is slightly reduced from 1.8 to 1.5  $\mu\text{m}$ , D50 goes from 3.3 to 2.6  $\mu\text{m}$  and D90 shrinks from 7.4 to 4.7  $\mu\text{m}$ . This is also apparent on the average size of the particles, and most importantly on the standard deviation on the particle size distribution; when using 3 mm grinding media, the standard deviation is only 1.4  $\mu\text{m}$  compared to 2.6  $\mu\text{m}$  for the 10 mm media. The standard deviation is representative of the width of the particle size distribution and is expected for planetary ball milling, as using smaller grinding media reduces the size of the particles.

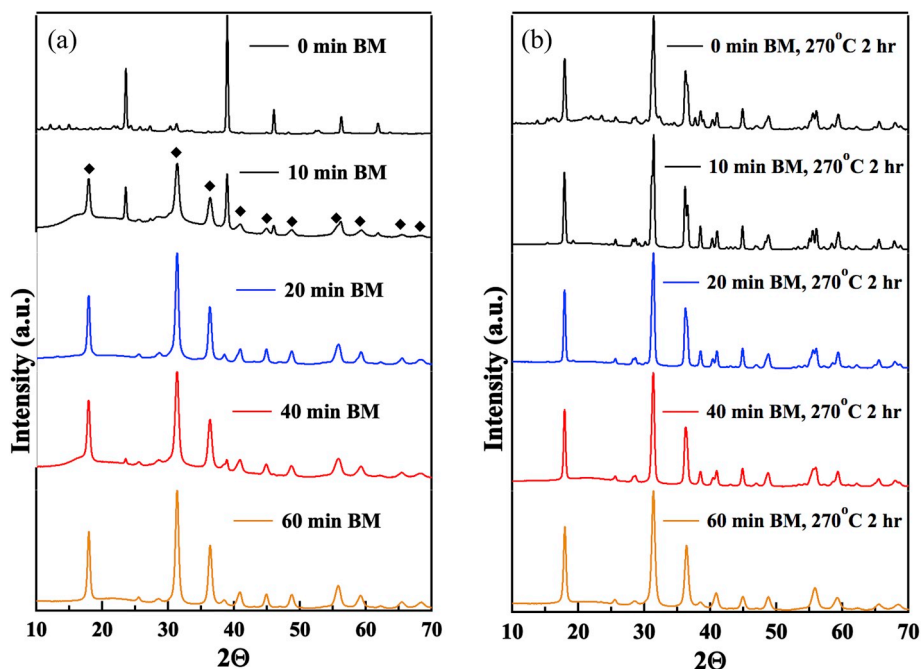


Fig. 4. XRD patterns of 75Na<sub>2</sub>S–25P<sub>2</sub>S<sub>5</sub> mixtures at various milling times (a) without and (b) with heat treatment at 270 °C for 2 h. Markers indicate peaks belonging to the Na<sub>3</sub>PS<sub>4</sub> phase.

### 3.3. Heat treatment

In this work, we show that a crystalline Na<sub>3</sub>PS<sub>4</sub> phase is formed during the ball milling process alone, achieving the desired material structure and conductivity without subsequent heat treatment. However, Hayashi et al. suggested that heat treatment of the amorphous phase (produced from the ball milling process) was necessary to form a crystalline structure [26]. This was explained to be an important process as the highly conductive cubic Na<sub>3</sub>PS<sub>4</sub> could be only formed via low temperature heating, contrary to findings by Jansen et al. To investigate whether further heat treatment is needed once the formation stage has been completed, a structural comparison of ball-milled 75Na<sub>2</sub>S–25P<sub>2</sub>S<sub>5</sub>, without heat treatment and with subsequent heat treatment, was collected with XRD and shown in Fig. 4a and b, respectively. In the case where the starting precursors are only mixed, *i.e.* no ball milling, heating the mixture to 270 °C for two hours resulted in the formation of tetragonal Na<sub>3</sub>PS<sub>4</sub> with additional unidentified impurities. Na<sub>2</sub>S is not found to be present in the XRD measurement and is believed to be completely consumed. The tetragonal polymorph is apparent in the XRD plot, as the signature peak splitting is present and caused by the c-lattice

asymmetry compared with the cubic structure. In contrast, when the starting material is ball milled, as previously demonstrated, Na<sub>3</sub>PS<sub>4</sub> is formed in the first ten minutes of ball milling as seen in Fig. 4a. The peaks of Na<sub>2</sub>S are identified in the sample that was ball milled for ten minutes, while the P<sub>2</sub>S<sub>5</sub> peaks are believed to be amorphous and only detectable with Raman. Subsequently, the mixture having been ball milled for ten minutes, was heated at 270 °C for two hours and the resulting product was found to be mostly tetragonal Na<sub>3</sub>PS<sub>4</sub>. The remaining milled samples were subjected to heating, and similarly, tetragonal Na<sub>3</sub>PS<sub>4</sub> can be observed at up to forty minutes in Fig. 4b. However, it can be seen that as ball milling progresses before the heat treatment, features of tetragonal Na<sub>3</sub>PS<sub>4</sub> is reduced and more cubic Na<sub>3</sub>PS<sub>4</sub> remains, when the samples are heated.

When the Saturation stage is reached after sixty minutes of ball milling, the main phase observed is cubic Na<sub>3</sub>PS<sub>4</sub>, as shown in Fig. 4a. Fig. 4b shows that subsequent heat treatment of this sixty-minute ball-milled mixture does not result in any impurities nor structural changes as opposed to mixtures that were subjected to shorter ball milling times, *i.e.* mixtures still in the Formation stage. Saturation is thus synonymous with the complete consumption of the starting precursors; none remain

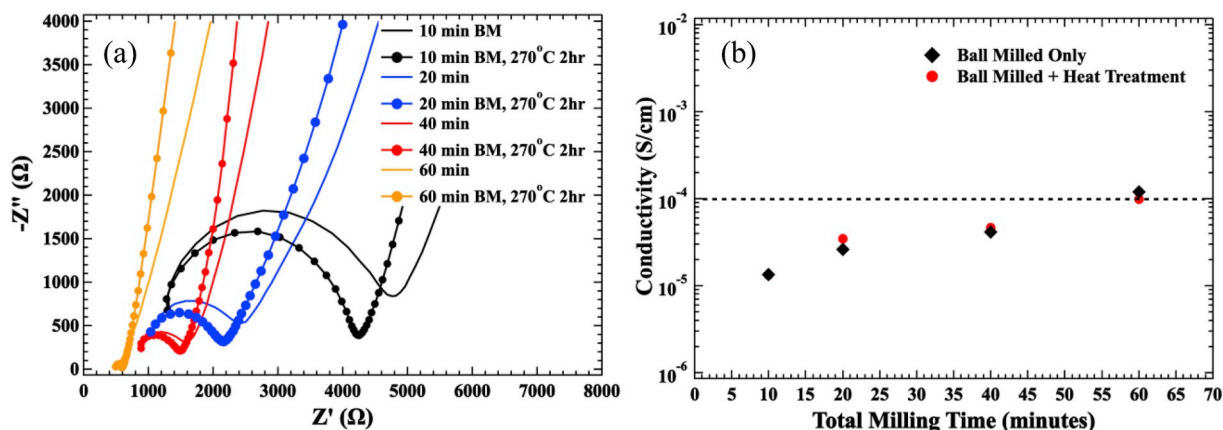


Fig. 5. (a) Nyquist plots and (b) corresponding conductivity measurements of 75Na<sub>2</sub>S–25P<sub>2</sub>S<sub>5</sub> ball milled mixtures with and without heat treatment.

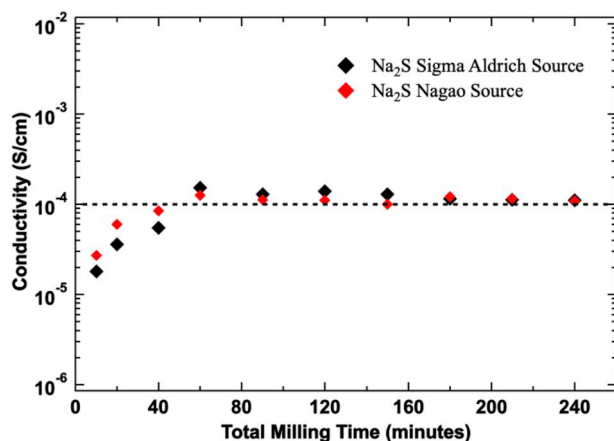


Fig. 6. Ionic conductivity comparison of  $\text{Na}_3\text{PS}_4$  made with  $\text{Na}_2\text{S}$  sourced from Sigma Aldrich (98%) and Nagao (99.6%).

to form tetragonal  $\text{Na}_3\text{PS}_4$  upon subsequent heat treatment. According to Fig. 4b, if non-ball-milled  $\text{Na}_2\text{S}$  and  $\text{P}_2\text{S}_5$  remain and are directly heated to  $270^\circ\text{C}$ , tetragonal  $\text{Na}_3\text{PS}_4$  forms. However, ball milling forms majority cubic  $\text{Na}_3\text{PS}_4$  and it is interesting to note that once the cubic phase forms, the phase transition from cubic to tetragonal appears to be kinetically limited even at elevated temperatures. These results are also supported by the Rietveld refinement results in Fig. S2 and Table S1.

A comparison of the material's overall ionic conductivity when subjected to ball milling, with and without heat treatment, is shown in Fig. 5a and b. When the material is only ball milled, its overall conductivity follows the same progression discussed earlier and a maximum conductivity is achieved when the Saturation stage is reached. However, subsequent heat treatment of the ball-milled material does not have a significant effect on the material's overall conductivity at each milling and heating interval. When the mixture is ball milled for ten minutes and heated, its  $\text{Na}^+$  conductivity does not differ from the mixture subjected to only ball milling. Similar results were measured from the samples subjected to further synthesis, where ball milling only or ball milling with heating does not significantly alter the SSE conductivity. The measured conductivity is likely from the cubic phase, which has remained after ball milling and heating and the progressive increase in conductivity reflects the larger percentage of cubic  $\text{Na}_3\text{PS}_4$  formed from the milling process. Therefore, the results in this work strongly suggest that synthesis of highly conductive  $\text{Na}_3\text{PS}_4$  can be achieved through a one-step ball milling process without any subsequent processing.

### 3.4. Sources of the $\text{Na}_2\text{S}$ reactant

The final parameter that was varied is the source of  $\text{Na}_2\text{S}$ , or the purity of  $\text{Na}_2\text{S}$ . This has been argued to critically affect the properties of  $\text{Na}_3\text{PS}_4$  [26], where high-purity  $\text{Na}_2\text{S}$  was suggested to produce high

$\text{Na}^+$  conductivity. A comparison of the SSE conductivity synthesized from different precursor sources was tracked and shown in Fig. 6. It can be seen that the synthesis trend between  $\text{Na}_2\text{S}$  sourced from Nagao (99.6%) or Sigma Aldrich (98%) are similar. The purity of the  $\text{Na}_2\text{S}$  source is found to not have a significant influence on the ionic conductivity of the synthesized  $\text{Na}_3\text{PS}_4$ .

### 3.5. Electrochemical performance evaluation

While the ionic conductivity ( $\sigma_i$ ) of SSEs is an important property to evaluate how quickly the material can shuttle ions between electrodes, its electronic conductivity ( $\sigma_e$ ) is an equally important but commonly overlooked characteristic. An ideal SSE should have a  $\sigma_e$  several orders of magnitude lower than its  $\sigma_i$ . Here, we measure the electronic conductivity by polarizing the synthesized SSE to a series of different potentials and holding at these potentials until a steady state current response is reached. The non-zero steady state current of the SSE with Ti blocking electrodes represents the electronic conductivity of  $\text{Na}_3\text{PS}_4$ . The linear response in the I–V relation is plotted in Fig. 7a and the  $\sigma_e$  was determined from this slope. The  $\sigma_i$  was found to be six-orders of magnitude larger than the  $\sigma_e$ , and the comparison is shown in Fig. 7b. The large difference between the two transport properties of the SSE makes it an ideal electrolyte material.

The performance of  $\text{Na}_3\text{PS}_4$  was also evaluated in an all-solid-state battery using  $\text{TiS}_2$  and a  $\text{Na}_{15}\text{Sn}_4$  alloy as the cathode and anode, respectively. The first charge and discharge cycle is shown in Fig. 8a where the ASSB was able to deliver  $185\text{ mAh g}^{-1}$  on the first discharge. The ASSB rate performance was also evaluated and shown in Fig. 8b. The ASSB is able to deliver a discharge capacity of 153, 138, 115, and  $75\text{ mA g}^{-1}$  when subjected to current densities of 126, 189, 378, and  $945\text{ }\mu\text{A cm}^{-2}$ , respectively. These results, in combination with the previous characterization results, show that  $\text{Na}_3\text{PS}_4$ , synthesized in this work by single-step ball milling, has proven to be functional as a SSE in an all-solid-state sodium ion battery.

## 4. Conclusions

Existing literature reports on  $\text{Na}_3\text{PS}_4$  solid electrolyte synthesis shows large variations in synthesis conditions, all of which is achieved with multiple synthesis steps. Through systematic investigation of the various key synthesis parameters, we demonstrated that cubic  $\text{Na}_3\text{PS}_4$  synthesis can be achieved in a single step. This is done by identifying the Formation and Saturation stages of  $\text{Na}_3\text{PS}_4$  synthesis; once Saturation is reached, the reaction to form highly conductive  $\text{Na}_3\text{PS}_4$  has completed and any additional processing has no effect on the material's conductivity or structural properties. The completion rate of the Formation stage is dependent on the rotational speed and grinding media size used during the milling process. Finally, electrochemical cycling of a  $\text{Na}_{15}\text{Sn}_4|\text{NPS}|\text{TiS}_2$  cell demonstrates that  $\text{Na}_3\text{PS}_4$  can be synthesized in a facile one-step process and that subsequent heat treatment is not critical.

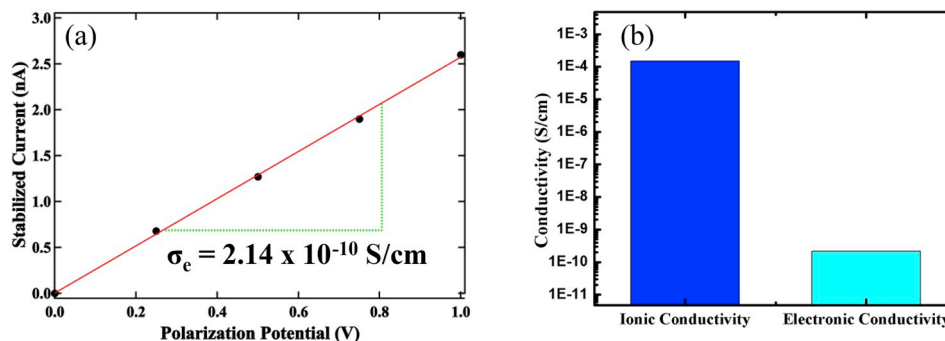


Fig. 7. (a) Electronic conductivity of  $\text{Na}_3\text{PS}_4$ . (b) Ionic and electronic conductivity comparison of  $\text{Na}_3\text{PS}_4$ .

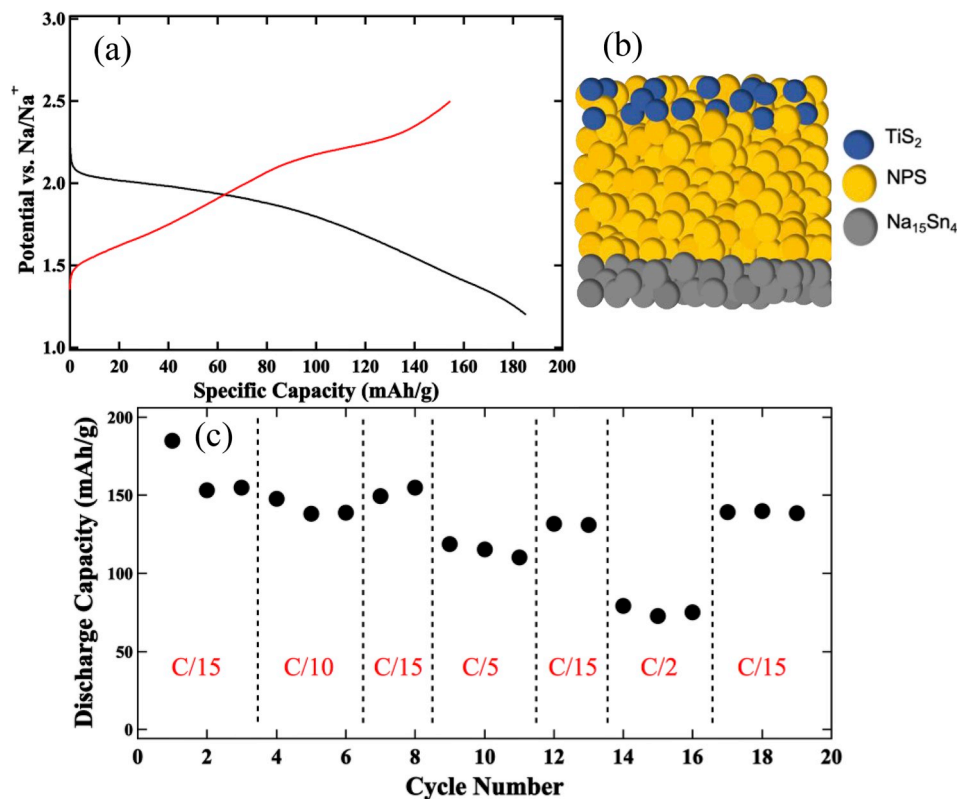


Fig. 8. (a) Potential curve at the first cycle, (b) diagram of all-solid-state battery construction, and (c) rate performance of  $\text{Na}_3\text{PS}_4$  in an all-solid-state battery. Current density to C-rate are:  $126 \mu\text{A cm}^{-2}$  (C/15),  $189 \mu\text{A cm}^{-2}$  (C/10),  $378 \mu\text{A cm}^{-2}$  (C/5),  $945 \mu\text{A cm}^{-2}$  (C/2).

A one-step, scalable ball-milling process is favorable for production of large batch sizes of solid-state electrolyte, one essential aspect for commercial viability.

#### Acknowledgements

Funding to support this work was provided by the Energy & Biosciences Institute through the EBI-Shell program contract number PT78832.

We thank Dr. Curtis Moore and Dr. Milan Gembicky at the Crystallography Facility at the University of California, San Diego for assisting on the capillary XRD data collection. The characterization work was performed in part at the San Diego Nanotechnology Infrastructure (SDNI), a member of the National Nanotechnology Coordinated Infrastructure, which is supported by the National Science Foundation under Grant PT78832.

\*The authors declare no competing financial interest.

#### Appendix A. Supplementary data

Supplementary data to this article can be found online at <https://doi.org/10.1016/j.jpowsour.2019.05.031>.

#### References

- [1] Z. Gao, H. Sun, L. Fu, F. Ye, Y. Zhang, W. Luo, Y. Huang, Promises, challenges, and recent progress of inorganic solid-state electrolytes for all-solid-state lithium batteries, *Adv. Mater.* (2018), 1705702, <https://doi.org/10.1002/adma.201705702>.
- [2] A. Manthiram, X. Yu, S. Wang, Lithium battery chemistries enabled by solid-state electrolytes, *Nat. Rev. Mater.* 2 (2017) 16103, <https://doi.org/10.1038/natrevmats.2016.103>.
- [3] N. Kamaya, K. Homma, Y. Yamakawa, M. Hirayama, R. Kanno, M. Yonemura, T. Kamiyama, Y. Kato, S. Hama, K. Kawamoto, A. Mitsui, A lithium superionic conductor, *Nat. Mater.* 10 (2011) 682–686, <https://doi.org/10.1038/nmat3066>.
- [4] A.A. Borsa, H.A. Fricker, B.G. Bills, J. Minster, C.C. Carabajal, K.J. Quinn, Topography of the salar de Uyuni, Bolivia from kinematic GPS, 2008, pp. 31–40, <https://doi.org/10.1111/j.1365-246X.2007.03604.x>.
- [5] L.A. Munk, S.A. Hynek, D. Bradley, D. Boutt, K. Labay, H. Jochens, Lithium brines: a global perspective, *Rev. Econ. Geol.* 18 (2016) 339–365.
- [6] H. Pan, Y.S. Hu, L. Chen, Room-temperature stationary sodium-ion batteries for large-scale electric energy storage, *Energy Environ. Sci.* 6 (2013) 2338–2360, <https://doi.org/10.1039/c3ee40847g>.
- [7] J.B. Goodenough, H.Y.-P. Hong, J. a. Kafalas, Fast  $\text{Na}^+$  - Ion Transport in Skeleton Structures, vol. 1, 1976, pp. 203–220, [https://doi.org/10.1016/0025-5408\(76\)90077-5](https://doi.org/10.1016/0025-5408(76)90077-5).
- [8] Alan S. Nagelberg, Wayne L. Worrell, A thermodynamic study of sodium-intercalated  $\text{TaS}_2$  and  $\text{TiS}_2$ , *J. Solid State Chem.* 29 (3) (1979) 345–354.
- [9] J.P. Parant, R. Olazcuaga, M. Devalette, C. Fouassier, P. Hagenmuller, Sur quelques nouvelles phases de formule  $\text{Na}_x\text{MnO}_2$  ( $x \leq 1$ ), *J. Solid State Chem.* 3 (1) (1971) 1–11.
- [10] C. Delmas, C. Fouassier, P. Hagenmuller, Structural classification and properties of the layered oxides, *Phys. B+C* 99 (1980) 81–85, [https://doi.org/10.1016/0378-4363\(80\)90214-4](https://doi.org/10.1016/0378-4363(80)90214-4).
- [11] J.J. Braconnier, C. Delmas, C. Fouassier, P. Hagenmuller, Comportement electrochimique des phases  $\text{Na}_x\text{CoO}_2$ , *Mater. Res. Bull.* 15 (12) (1980) 1797–1804.
- [12] M.S. Whittingham, Chemistry of Intercalation Compounds: Metal Guests in Chalcogenide Hosts, 1978, [https://doi.org/10.1016/0079-6786\(78\)90003-1](https://doi.org/10.1016/0079-6786(78)90003-1).
- [13] B.L. Ellis, L.F. Nazar, Sodium and sodium-ion energy storage batteries, *Curr. Opin. Solid State Mater. Sci.* 16 (2012) 168–177, <https://doi.org/10.1016/j.cossms.2012.04.002>.
- [14] K.B. Hueso, M. Armand, T. Rojo, High temperature sodium batteries: status, challenges and future trends, *Energy Environ. Sci.* 6 (2013) 734, <https://doi.org/10.1039/c3ee24086j>.
- [15] H.-P. Hong, Crystal structures and crystal chemistry in the system  $\text{Na}_{1+x}\text{Zr}_2\text{Si}_x\text{P}_{3-x}\text{O}_{12}$ , *Mater. Res. Bull.* 11 (1976) 173–182, [https://doi.org/10.1016/0025-5408\(76\)90073-8](https://doi.org/10.1016/0025-5408(76)90073-8).
- [16] I.O.N. Conductors, B.O.N. Nasicon, Takehiko TAKAHASHI, Katsumi KUWABARA and Masahiro SHIBATA 1 (1980) 163–175.
- [17] T. Wheat Ahmad, a Kuriakose, J. Canaday, a McDonald, Dependence of the properties of Nasicons on their composition and processing, *Solid State Ionics* 24 (1987) 89–97, [https://doi.org/10.1016/0167-2738\(87\)90070-1](https://doi.org/10.1016/0167-2738(87)90070-1).
- [18] M. Jansen, U. Henseler, Synthesis, structure determination, and ionic conductivity of sodium tetrathio phosphate, *J. Solid State Chem.* 99 (1992) 110–119, [https://doi.org/10.1016/0022-4596\(92\)90295-7](https://doi.org/10.1016/0022-4596(92)90295-7).
- [19] A. Hayashi, K. Noi, A. Sakuda, M. Tatsumisago, Superionic glass-ceramic electrolytes for room-temperature rechargeable sodium batteries, *Nat. Commun.* 3 (2012) 856, <https://doi.org/10.1038/ncomms1843>.

- [20] T. Krauskopf, S.P. Culver, W.G. Zeier, Local Tetragonal Structure of the Cubic Superionic Conductor  $\text{Na}_3\text{PS}_4$ , 2018, pp. 4–9, <https://doi.org/10.1021/acs.inorgchem.8b00458>.
- [21] T. Krauskopf, C. Pompe, M.A. Kraft, W.G. Zeier, Influence of lattice dynamics on  $\text{Na}^+$  transport in the solid electrolyte  $\text{Na}_3\text{PS}_{4-x}\text{Se}_x$ , *Chem. Mater.* 1 (2017), <https://doi.org/10.1021/acs.chemmater.7b03474>.
- [22] N. Tanibata, M. Deguchi, A. Hayashi, M. Tatsumisago, All-solid-state Na/S batteries with a  $\text{Na}_3\text{PS}_4$  electrolyte operating at room temperature, *Chem. Mater.* 29 (2017) 5232–5238, <https://doi.org/10.1021/acs.chemmater.7b01116>.
- [23] N. Tanibata, T. Matsuyama, A. Hayashi, M. Tatsumisago, All-solid-state sodium batteries using amorphous TiS<sub>3</sub> electrode with high capacity, *J. Power Sources* 275 (2015) 284–287, <https://doi.org/10.1016/j.jpowsour.2014.10.193>.
- [24] N. Tanibata, K. Noi, A. Hayashi, N. Kitamura, Y. Idemoto, M. Tatsumisago, X-ray crystal structure analysis of sodium-ion conductivity in  $94\text{Na}_3\text{PS}_4 \cdot 6\text{Na}_4\text{Si}_3\text{S}_{12}$  glass-ceramic electrolytes, *ChemElectroChem* 1 (2014) 1130–1132, <https://doi.org/10.1002/celec.201402016>.
- [25] T. Yamanaka, A. Yamauchi, A. Hayashi, M. Tatsumisago, Preparation of Sodium Ion Conducting  $\text{Na}_3\text{PS}_4\text{-NaI}$  Glasses by a Mechanochemical Technique, vol. 270, 2015, pp. 6–9, <https://doi.org/10.1016/j.ssi.2014.11.024>.
- [26] A. Hayashi, K. Noi, N. Tanibata, M. Nagao, M. Tatsumisago, High sodium ion conductivity of glass-ceramic electrolytes with cubic  $\text{Na}_3\text{PS}_4$ , *J. Power Sources* 258 (2014) 420–423, <https://doi.org/10.1016/j.jpowsour.2014.02.054>.
- [27] H. Wan, J.P. Mwiszerwa, X. Qi, X. Xu, H. Li, Q. Zhang, L. Cai, Y.-S. Hu, X. Yao, Nanoscaled  $\text{Na}_3\text{PS}_4$  solid electrolyte for all-solid-state  $\text{FeS}_2/\text{Na}$  batteries with ultrahigh initial coulombic efficiency of 95% and excellent cyclic performances, *ACS Appl. Mater. Interfaces* (2018), <https://doi.org/10.1021/acsami.8b01805>.
- [28] S. Wenzel, T. Leichtweiss, D.A. Weber, J. Sann, W.G. Zeier, J. Janek, Interfacial reactivity benchmarking of the sodium ion conductors  $\text{Na}_3\text{PS}_4$  and sodium  $\beta$ -alumina for protected sodium metal anodes and sodium all-solid-state batteries, *Appl. Mater. Interfaces* (2016), <https://doi.org/10.1021/acsami.6b10119>.
- [29] J. Yue, F. Han, X. Fan, X. Zhu, Z. Ma, J. Yang, C. Wang, High-performance all-inorganic solid-state sodium-sulfur battery, *ACS Nano* 11 (2017) 4885–4891, <https://doi.org/10.1021/acs.nano.7b01445>.
- [30] Z. Yu, S.-L. Shang, J.-H. Seo, D. Wang, X. Luo, Q. Huang, S. Chen, J. Lu, X. Li, Z.-K. Liu, D. Wang, Exceptionally high ionic conductivity in  $\text{Na}_3\text{P}_{0.62}\text{As}_{0.38}\text{S}_4$  with improved moisture stability for solid-state sodium-ion batteries, *Adv. Mater.* (2017), 1605561, <https://doi.org/10.1002/adma.201605561>.
- [31] C. Yu, S. Ganapathy, N.J.J. de Klerk, E.R.H. van Eck, M. Wagemaker, Na-ion dynamics in tetragonal and cubic  $\text{Na}_3\text{PS}_4$ , A Na-ion conductor for solid state Na-ion batteries, *J. Mater. Chem. A* 4 (2016) 15095–15105, <https://doi.org/10.1039/C6TA05896E>.
- [32] Allen C. Larson, Robert B. Von Dreele, "Gsas." Report IAU, 1994, pp. 86–748.
- [33] Brian H. Toby, EXPGUI, a graphical user interface for GSAS, *J. Appl. Crystallogr.* 34 (2) (2001) 210–213.
- [34] E.A. Wu, C.S. Kompella, Z. Zhu, J.Z. Lee, S.C. Lee, I.H. Chu, H. Nguyen, S.P. Ong, A. Banerjee, Y.S. Meng, New insights into the interphase between the Na metal anode and sulfide solid-state electrolytes: a joint experimental and computational study, *ACS Appl. Mater. Interfaces* 10 (12) (2018) 10076–10086.
- [35] S.S. Berbano, I. Seo, C.M. Bischoff, K.E. Schuller, S.W. Martin, Formation and structure of  $\text{Na}_2\text{S} + \text{P}_2\text{S}_5$  amorphous materials prepared by melt-quenching and mechanical milling, *J. Non-Cryst. Solids* 358 (2012) 93–98, <https://doi.org/10.1016/j.jnoncrysol.2011.08.030>.